Randomized Self-Structuring Adaptive Neuro-Fuzzy Based Induction Motor Drives With Optimized FOPI Gains

Pudari MAHESH and Sabha Raj ARYA

***Abstract*—This paper describes the randomized evolving Takagi-Sugeno (ReTSK)-adaptive neuro-fuzzy (ANF) estimation algorithm and optimized fractional-order proportional integral (FOPI) controller are integrated with parameter adaptive indirect vector control (PA-IVC) for induction motor drives performance enhancement. For appropriate slip-speed tuning and field orientation, the machine learning-based ReTSK-ANF approach is proposed for the estimation of induction motor parameters and sensorless speed. The optimized FOPI speed and current regulators are employed in PA-IVC to generate the reference signals with minimized error for encountering manual tuning and reduce the overshoot with less settling time. A metaheuristic algorithm of Gazelle optimization algorithm (GOA) is imposed, to obtain the optimal weight, biases, membership functions (MFs), and MF rules in the predicative model of ReTSK-ANF for desired parameter estimation and optimal gains of FOPI for performance enhancement. Statistical metrics are carried out to examine the performance of ReTSK forecasting model. The metrics are mean square error (MSE), root mean square error (RMSE), mean error (ME), and error of standard deviation (ESD) as reportd during the training stage, were 3.33e-3, 3.41e-2, 1.92e-3, 3.37e-2, and during the testing stage 3.67e-3, 3.47e-2, 1.91e-3, 3.42e-2. This will confirm that the ReTSK-ANF estimator will achieve significant improvement in the estimation of parameters and closely follow the reference. Meanwhile, the optimized FOPI gains performance is analyzed using time response analysis.**

***Index Terms*—Adaptive neuro-fuzzy (ANF), adaptive parameter estimation, fractional order proportional integral (FOPI), Gazelle optimization algorithm (GOA), induction motor drives (IMD), indirect vector control (IVC), randomized evolving takagisugeno (ReTSK), statistical metrics.**

I. Introduction

TO achieve the greater dynamic effectiveness of induction motor drives (IMD), a well-known control approach is entitled as indirect vector control (IVC) [1]. Due to its straight forward design, quicker dynamic reaction, increased noise immunity, and compatibility with harsh environments. It inherently consists of speed as feedback and is susceptible to changes in the parameters [2]. Various classical sensorless speed control strategies are reviewed in [3], [4]. The high-effectiveness drives need precise information on machine speed as well as electrical parameters, because of thermal, skin, and saturation effects on machine parameters during operation [5].

To enhance the drive performance with proper field orientation, accurate parameter estimation is necessary in automotive and industrial applications [6]. As demonstrated earlier, plenty of work has been carried out on sensorless speed control of IMDs through parameter estimation. In [7], rotor time constant estimation with adaptive IVC for slip speed tuning based on unified model reference adaptive system (MRAS) strategy, and in [8] based on adaptive law MRAS is implemented for mutual inductance estimation. Although it is feasible to employ, an adaptive rate's architecture is intricate. An integral calculation-based method for the estimate of the magnetizing inductance and rotor constant time constant at a standstill was proposed by Lee *et al.* [9]. For low inertia-based drive applications, the DC signal injected method is developed for stator resistance estimation [10]. Which consists of the differentiation of current signals, due to high harmonic content the differentiation will not properly estimate the parameters. For evaluation of the rotor time constant flux decay test is proposed by Eric *et al.* in [11]. However, it fails to properly tune the slip speed for accurate field orientation, as the slip speed depends on induction motor (IM) parameters. Classical control strategies have limitations in estimating all parameters, leading to increased system complexity. Consequently, these approaches may not provide accurate slip speed and field orientation, which can degrade the performance of the IMD.

Artificial intelligence (AI) control techniques are developed in drive applications to reduce the complexity and computation burned with faster convergence [12]. Because of their high processing speed, capacity for learning, and adaptability, AI is convenient for adaptive control systems. In [13], feed-forward multilayer perceptron and Elman recurrent neural network (ERNN) are developed for the correction of estimated speed for sensorless operation IM. Equivalent circuit parameters of IM are estimated by using ERNN [14], and AdaDelta rule-based backpropagation neural network (NN) [15]. For rotor time constant estimation fuzzy

Manuscript received June 16, 2024; revised October 27, 2024; accepted November 17, 2024. Date of publication December 30, 2024; date of current version November 27, 2024. No funding was received to assist with the preparation of this manuscript. *(Corresponding author: Sabha Raj Arya.)*

Both authors are with the Department of Electrical Engineering, Sardar Vallabhbhai National Institute of Technology, Surat-395007, India (e-mail: mahe.nani64@gmail.com; sabharaj79@gmail.com).

Digital Object Identifier 10.24295/CPSSTPEA.2024.00026

method is proposed by Zidani *et al.* in [16]. The fuzzy system cannot learn or adapt to different environments, while NN is often incomprehensible to users. By integrating the two, a hybrid intelligence algorithm, the adaptive neurofuzzy (ANF) system, is developed. This integration makes the NN more transparent and enhances the fuzzy system's learning capability. ANF can offer more accurate responses for a high-order dynamic system with quick convergence speed. In general, ANF system premise and consequence parameters are determined by gradient descent (GD), and least square estimation (LSE), but they may not be optimal for the predictor model [17]. The ML-based ANF system is implemented to enhance performance and stability [18]. Particle swarm optimisation (PSO) is used to design the optimal adaptive neuro-fuzzy inference system (ANFIS) model in [19], GA, and PSO-ANFIS for brushless DC (BLDC) speed estimation in [20]. To avoid the manual selection of fuzzy rules and membership functions (MFs) in a fuzzy, and choosing the weight and biases in NN the optimization is employed [21]. The new gradient-free optimization of GOA demonstrates its efficacy when the controller's coefficient is tuned [22]. GOA is utilized in the control design for simultaneous online tuning of the premise and consequent parameters, MFs, and optimal rule selection.

A key component of the controller is the gain tuning of fractional order proportional integral (FOPI) coefficients, which enhances the tracking capability of the reference value and improves robustness against disturbances while reducing oscillations and overshoot. The author is particularly interested in optimizing FOPI-based IVC-IMD using advanced meta-heuristic techniques for fine-tuning FOPI coefficients. Various advanced meta-heuristic optimization techniques have been employed for fine-tuning FOPI coefficients [18], [23], with PSO being one of the most recommended methods for gain tuning. However, PSO is prone to local entrapment, necessitating modifications to address the problem's complexity [24]. To mitigate these drawbacks, other modern optimization techniques have also been explored for gain tuning of FOPI coefficients, including Harris Hawks optimization [25], and Gray Wolf optimizer algorithm [26]. These methods minimize the computational effort required for coefficient tuning and improve dynamic response. GOA effectively focuses on standard control parameters, reduces local optima risks, and enhances convergence [27]. The GOA-based FOPI tuning approach surpasses previous methods by achieving optimal FOPI coefficient values and superior dynamic response and stability, with the integral time square error (ITSE) error rate function optimizing settling time and minimizing oscillations.

This study primarily analyzes the performance of a self-learning randomized evolving takagi-sugeno (ReTSK) model for online parameter identification of IMD. The GOA, inspired by the survival strategies of gazelles in predator-dominated environments, serves as an efficient metaheuristic for developing the ReTSK-ANF model. GOA optimizes both the structure and parameters of unknown system dynamics, allowing the ReTSK to estimate multiple parameters accurately while minimizing oscillations through adaptive adjustments of MFs and fuzzy rules. For effective field orientation and slip speed tuning in IVC, the estimated parameters from the ReTSK-ANF model are used. A FOPI controller is employed to enhance dynamic performance, leveraging the additional fractional integrator coefficient (λ) for quicker adaptation and settling to a steady state. GOA also optimizes the FOPI gains, achieving optimal values with reduced computational effort. The performance of the PA-IVC-IMD using optimal FOPI gains is assessed through MATLAB/Simulink and validated via experimental testing.

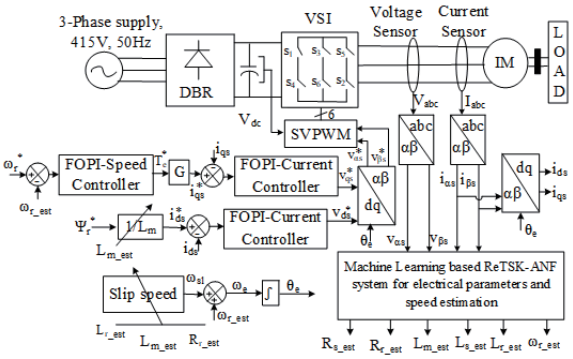

Fig. 1. Schematic diagram of proposed control algorithm for IMDs.

II. System Configuration

A three-phase squirrel cage rotor type of induction motor using parameter adaptive indirect vector control (PA-IVC) strategy configuration is demonstrated in Fig. 1. The IVC-IMD sensorless speed control is implemented with an optimized FOPI controller and ML-based ReTSK. It is employed for the simultaneous estimation of parameters and sensorless speed of IM. By adopting these parameters in the control strategy, the slip speed is computed for the appropriate evolution of field orientation.

The architecture that is being demonstrated includes a detailed overview of each significant component associated with the IMD. Three-phase supply is given as input to the three-phase diode bridge rectifier (DBR). The three-phase rectifier output voltage is given to the voltage source inverter (VSI) through a DC-link capacitor (C_d). The stationary reference frame and DC-link voltages are fed as input to space vector pulse width modulation (SVPWM) for the generation of the switching pulses. IM is operated according to the controller's instructions involved in the PA-IVC drive system. FOPI controllers are adopted in the IVC to enhance the drive dynamic performance with reduced settling time and ripples for the generation of reference voltages as per the speed and load changes for excellent dynamic drive operation. The system specifications are reported in an Appendix.

III. Control Strategy

The proposed PA-IVC for IMD integrates key components to address dynamic parametric uncertainties. First, a machine learning-based ReTSK-ANF model is employed for concurrent parameter and sensorless speed estimation, by adopting the estimated parameters in IVC to adjust slip speed and field

orientation. Second, a metaheuristic optimization algorithm is employed for fine-tuning FOPI gains in speed and current regulators. GOA is independently implemented to optimize the predictor model and FOPI gains. The control algorithms are theoretically and mathematically detailed in this section.

A. Mathematical Model of IVC-Based Dynamic IMD

An IM dynamic model based on a stationary reference frame is as follows [1]:

$$\begin{bmatrix} v_{\alpha s} \\ v_{\beta s} \\ 0 \\ 0 \end{bmatrix} = \begin{bmatrix} R_s + \rho L_s & 0 & \rho L_m & 0 \\ 0 & R_s + \rho L_s & 0 & \rho L_m \\ \rho L_m & \omega_r L_m & R_r + \rho L_r & \omega_r L_r \\ -\omega_r L_m & \rho L_m & -\omega_r L_r & R_r + \rho L_r \end{bmatrix} \begin{bmatrix} i_{\alpha s} \\ i_{\beta s} \\ i_{\alpha r} \\ i_{\beta r} \end{bmatrix} \quad (1)$$

The produced electromagnetic and generalized torque expression of the induction motor are given as:

$$\begin{cases} T_e = T_L + J \dfrac{d\omega_m}{dt} \\ T_{em} = \dfrac{3}{2} \cdot \dfrac{P}{2} \dfrac{L_m}{L_r} (i_{\beta s} \psi_{\alpha r} - i_{\alpha s} \psi_{\beta r}) \end{cases} \quad (2)$$

The q- and d-axis reference currents mathematical expression are given as:

$$\begin{cases} i_{qs}^{*} = \dfrac{4}{3p} \cdot \dfrac{L_r}{L_m} \cdot T_e^{*} \\ i_{ds}^{*} = \dfrac{\Psi_r}{L_m} \end{cases} \quad (3)$$

In IVC, the angular field position is computed employing the slip speed and rotor speed. The field angle (θ) and slip speed (ω_{sl}) are expressed as [2]

$$\begin{cases} \theta = \int (\omega_r + \omega_{sl}) dt; \\ \omega_{sl} = \dfrac{L_m R_r}{\Psi_r^{*} L_r} \cdot i_{qs}^{*} \end{cases} \quad (4)$$

where $i_{\alpha s}$, $i_{\beta s}$ and $v_{\alpha s}$, $v_{\beta s}$ represent the stator currents and voltages in a stationary reference frame, $i_{\alpha r}$ and $i_{\beta r}$ represent stationary reference frame rotor currents, p is a number of pole pairs, ρ is derivative variable, and ω_m is the mechanical speed.

B. Electric Vehicle Dynamic Model

The motor is one of the main components of an electric vehicle (EV). The rotating force applied by the wheels to sustain the vehicle movement is denoted as load torque. It is provided to the motor based on various factors, such as tire size, weight, slope, terrain type, and desired acceleration. The motor speed is given as input to the EVDM and it develops the vehicle torque. The sum of various forces presents in the EV system such as rolling force (f_r), grade force (f_g), acceleration force (f_a), and aerodynamic drag force (f_{ad}) is considered as tractive effort (f_t). By multiplying tractive effort with wheel radius (r_{wheel}) then the required torque (T_v) will develop. The variable amount of vehicle torque T_v is developed by changing the tilt angle [2].

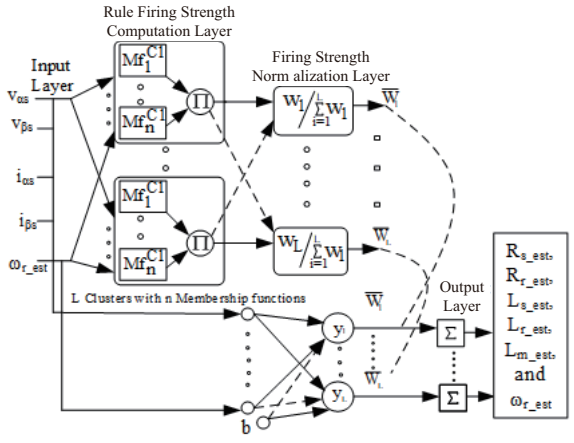

Fig. 2. Schematic diagram of ML-based ReTSK-ANF estimator.

$$\begin{cases} f_r = Mg\tau_r \cos\Phi; \;\; f_g = Mg \sin\Phi; \;\; f_a = Ma = M\dfrac{dV}{dt} \\ f_{ad} = 0.5\delta\tau_d A V^2; \;\; f_t = f_r + f_g + f_a + f_{ad} \\ T_v = r_{wheel} f_t \end{cases} \quad (5)$$

where M is gross weight, τ_r is rolling friction coefficient, g is acceleration gravity, Φ is gradient, a is acceleration, V is velocity of vehicle, δ is air density, τ_d is drag coefficient, and A is vehicle frontal area.

C. Development and Parameter Estimation Using the ReTSK-ANF System

Fig. 2 depicts the internal structure of ReTSK. Integrating the proposed strategy with the input space partitioning kernel FCM (K-FCM) approach improves convergence to produce the globally most effective solution [19], [22]. The inputs ($v_{\alpha s}$, $v_{\beta s}$, $i_{\alpha s}$, $i_{\beta s}$, and ω_r) to the ReTSK model and the Neurons in the next layer execute activation functions, it is obtained by the MFs of $\mu_j^i(x)$ where $x \in (v_{\alpha s}, v_{\beta s}, i_{\alpha s}, i_{\beta s}$, and $\omega_r)$. Weights and biases in a hidden layer are obtained arbitrarily in a randomized unit.

The ReTSK structure consists of the following layers: input, rule, MFs, and output. The meta-heuristic optimization technique Gazelle is adopted for the self-tuning of various coefficients of ReTSK such as rules, MFs numbers, and shape of MFs. Employing an inference rule-based system, the intended outputs (R_s, R_r, L_r, L_m, and ω_r) are obtained for variable inputs. By adopting GOA by tweaking the specified MFs till the error drops to the assigned value, the ReTSK generates an optimal set of rules that yield the optimal fuzzy inference system (FIS) [22]. The statistical metrics mean square error(MSE), root mean square error (RMSE), mean error (ME), and error of standard deviation (ESD) validate the expected outcomes. The

strategy for parameter estimation in the ReTSK module is derived as follows:

An overall output with hidden nodes (h_n), n distinct samples, and activation function $f(x)$ of the ReTSK-ANF system is expressed as:

$$\sum_{i=1}^{n} y_i k_i(x_j) = \sum_{i=1}^{n} y_i k(w_i x_j + b_j) = o_j,\ j = 1, 2, \ldots, n \quad (6)$$

where $w_i = [w_{i1}, w_{i2}, ..., w_{in}]^T$ is a weight vector between input nodes and jth middle layer, $y_i = [y_{i1}, y_{i2}, ..., y_{im}]^T$ is the output weight vector between middle nodes and the output linear node whilst b_i is the threshold of the ith hidden node. The existence parameters y_i, w_i and b_i $\sum_{i=1}^{n} y_i k(w_i x_j + b_j) = t_j$ for $j = 1, . ., n$, where t is the target weight vector. The middle layer neurons' weights (w_i) and bias (b_j) will be chosen as randomly to minimize the uncertainty in the proposed system. The output matrix H is defined as

$$Hy = T \quad (7)$$

where

$$H = \begin{bmatrix} k(w_1 \cdot x_1 + b_1 \cdots k(w_N \cdot x_1 + b_N) \\ \vdots \qquad \ddots \\ k(w_1 \cdot x_N + b_1) \ \vdots k(w_N \cdot x_N + b_N) \end{bmatrix}_{N \times N}; y = \begin{bmatrix} y_1^T \\ \vdots \\ y_N^T \end{bmatrix}_{N \times m}; T = \begin{bmatrix} t_1^T \\ \vdots \\ t_N^T \end{bmatrix}_{N \times m}$$

The output weight vector y_i is evaluated by solving.

The Moore-Penrose expanded inverse of matrix H is denoted by the notation H^{-1}. It offers the linear system described prior with the least-squares approach, and the resultant solution is distinct. For determining the linear system characteristic matrix y, use (6). The explicit comprehension contained within the linguistic variables represented in the premise portion of the fuzzy rules of ReTSK is employed to control the unpredictability [22]. If the antecedent component has been chosen for the specified input variables, then the H matrix is obtained by using (8).

$$T_{P \times 1} = H_{P \times m^n (n+1)} y_{m^n (n+1) \times 1} \quad (8)$$

The following illustrates the layer hierarchy and architecture of ReTSK-ANF:

Rule1: If $v_{\alpha s}$ is a_1, $v_{\beta s}$ is b_1, $i_{\alpha s}$ is c_1, $i_{\beta s}$ is d_1, ω_{r_est} is e_1, then $f_1 = g_1 v_{\alpha s} + h_1 v_{\beta s} + k_1 i_{\alpha s} + l_1 i_{\beta s} + o_1 \omega_{r\_est} + p_1$.

Rule 2: If $v_{\alpha s}$ is a_2, $v_{\beta s}$ is b_2, $i_{\alpha s}$ is c_2, $i_{\beta s}$ is d_2, ω_{r_est} is e_2, then $f_2 = g_2 v_{\alpha s} + h_2 v_{\beta s} + k_2 i_{\alpha s} + l_2 i_{\beta s} + o_2 \omega_{r\_est} + p_2$.

Rule 3: If $v_{\alpha s}$ is a_3, $v_{\beta s}$ is b_3, $i_{\alpha s}$ is c_3, $i_{\beta s}$ is d_3, ω_{r_est} is e_3, then $f_3 = g_3 v_{\alpha s} + h_3 v_{\beta s} + k_3 i_{\alpha s} + l_3 i_{\beta s} + o_3 \omega_{r\_est} + p_3$.

Rule 4: If $v_{\alpha s}$ is a_4, $v_{\beta s}$ is b_4, $i_{\alpha s}$ is c_4, $i_{\beta s}$ is d_4, ω_{r_est} is e_4, then $f_4 = g_4 v_{\alpha s} + h_4 v_{\beta s} + k_4 i_{\alpha s} + l_4 i_{\beta s} + o_4 \omega_{r\_est} + p_4$.

Rule 5: If $v_{\alpha s}$ is a_5, $v_{\beta s}$ is b_5, $i_{\alpha s}$ is c_5, $i_{\beta s}$ is d_5, ω_{r_est} is e_5, then $f_5 = g_5 v_{\alpha s} + h_5 v_{\beta s} + k_5 i_{\alpha s} + l_5 i_{\beta s} + o_5 \omega_{r\_est} + p_5$.

where g_i, h_i, k_i, l_i, o_i, and p_i are the linear consequent tunable parameters while a_i, b_i, c_i, d_i, e_i represent the premise parameters, and f_1, f_2, f_3, f_4, f_5 represent the output functions of the defined rules.

Layer 1: Inputs ($v_{\alpha s}$, $v_{\beta s}$, $i_{\alpha s}$, $i_{\beta s}$, and $\omega_{r\text{-}est}$) are assigned to this layer. In this case, MFs are utilized to determine the node outputs and rate each node based on the input signal. The output of node is given as:

$$O_{v_{\alpha s}}^2 = \mu_{ai\,(v_{\alpha s})},\ O_{v_{\beta s}}^2 = \mu_{bi\,(v_{\beta s})}, O_{i_{\alpha s}}^2 = \mu_{ci\,(i_{\alpha s})}, O_{i_{\beta s}}^2 = \mu_{di\,(i_{\beta s})}, O_{\omega_{\text{rest}}}^2 = \mu_{ei\,(\omega_{\text{rest}})} \quad (9)$$

where μ_{ai}, μ_{bi}, μ_{ci}, μ_{di}, and μ_{ei} represent the membership degrees concerning each input. To transform the input variable into a fuzzy rule, the GF has been used. It is given by (10).

$$\mu_{M_{ij}}(x) = \exp\left\{ -\frac{\left(x - \delta_{ij}\right)^2}{2\sigma_{ij}^2} \right\} \quad (10)$$

where δ_{ij} and σ_{ij} represent premises linear parameters, x denotes the respective input.

Layer 2: The AND or product action of the input MFs is carried out by this layer. The next node's input weight function is derived from the output of the product layer, it is given as:

$$O_i^3 = w_i = \mu_{ai(x)} AND\ \mu_{bi(x)}\ AND\ \mu_{ci(x)}\ AND\ \mu_{di(x)}\ AND\ \mu_{ei(x)} \quad (11)$$

Layer 3: This layer is assessed and normalizes the degree of rule activation.

$$O_i^4 = \overline{w_i} = \frac{w_i}{\sum_i w_i} \quad (12)$$

Layer 4: This is Defuzzification layer and each node in this layer is adaptive. The Sugeno functions (f_i) are also considered as inputs. The output of this layer is:

$$O_i^5 = \overline{w_i} f_i \quad (13)$$

The ReTSK model's ultimate output, which assesses the total of all outputs from the preceding layer, is provided as:

$$O_i^6 = \sum_i \overline{w_i} f_i \quad (14)$$

To achieve better system performance, the ReTSK parameters must be optimized. In this work, GOA-based supervised learning is developed to evaluate the parameters.

D. GOA Implementation

It is a meta-heuristic optimization inspired by gazelles' survival strategies in predator-dominated environments. The optimization process involves two key aspects: exploitation, represented by fleeing from sighted predators, and exploration, illustrated by grazing in their absence.

Exploitation phase: In this phase, gazelles are assumed to be either tracked by a predator or grazing peacefully in their absence. Their surroundings are efficiently covered through random motion, characterized by uniform and controlled steps. While grazing, the gazelles are assumed to move randomly, expressed mathematically as

$$G_{i+1} = G_i + vRR_b(Elite_i - R_b G_i) \quad (15)$$

where G_i is the position of the current iteration, G_{i+1} is the position of next iteration, v is grazing velocity, R_b is a random vector by random motion, and R is the random number [0,1].

Exploration phase: When a predator appears, the exploration phase begins. A gazelle's response to danger can be modeled by setting its height to a value between 0 and 1, twirling its tail, stomping its feet, or leaping up to 2 meters into the air. During this phase, Levy flight is employed to enhance search ability [27]. When the predator spots the gazelle, he pursues it, and both animals exhibit impulsive direction changes represented by ξ, which can occur at each iteration. The predator's actions as it chases the gazelle are represented mathematically as:

$$\vec{G}_{i+1} = \vec{G}_i + V\xi\kappa\vec{R}_b(\vec{Elite}_i - \vec{R}_l\vec{G}_i) \tag{16}$$

where $\kappa = (1 - iter / \max\_iter)^{(2iter/\max\_iter)}$ is the cumulative effect of a predator, V is the maximum velocity, and R_l is a random number based on Levy distributions.

The predator success rate is represented as ζ, and the gazelle can escape, which means the algorithm avoids being trapped in a local minimum [27].

GOA is employed in this research work with two main objectives sequentially. The first is to develop the optimal predictive ReTSK-ANF model, while the second focuses on determining optimal FOPI coefficients of speed and current controllers in IVC.

E. Learning of ReTSK and Objective Function Using GOA

An IMD control approach for parameter estimation uses the GOA to determine the fitness function. The GOA is motivated by gazelles' survival ability and its purpose is obtaining the optimal variables such as MFs, rules, and shape of MF [22]. If the obtained error approaches zero, then the estimated response strongly tracks the target. An error between actual and measured parameters is compared to evaluate an optimal predicted value (p), by considering it as a fitness function.

$$Objective\ function = RMSE = sqrt\left(\frac{1}{n}\sum_{k=1}^{n}(Y_{d\_k} - Y^*_{p\_k})^2\right) \tag{17}$$

It's indeed to determine the RMSE for each training sample. Where Y_{d_k} is the desired output of actual and $Y^*_{p\_k}$ is the predicted output of estimated parameters of IM with kth training sample and n is the number of training samples.

The new position calculated for each gazelle is acceptable for the update process if it improves the value of an objective function, otherwise, it remains in the same. The complete iterative learning process is replicated until it finds the best position (or max_*iter*) and checks the best feasible solutions.

F. FOPI-Based Speed and Current Regulator in PA-IVC

It is crucial to precisely estimate the appropriate values of reference signals in IVC when the speed and current variations are minimized by keeping actual values nearer to the reference. The obtained error is addressed by integrating the coefficients of FOPI with GOA. The metaheuristic algorithm such as GOA is adopted to precisely tune the FOPI gains for the determination of the reference signals such as torque component (T_e^*), d-axis voltage (v_{ds}^*), and q-axis voltage (v_{qs}^*). The three FOPI controllers fetched an error of input by comparing the reference and actual values of the receptive controller component such errors are speed error (ω_{re}), d-axis current errors (i_{ds_e}), and q-axis current errors (i_{qs_e}), respectively, which are expressed as:

$$\begin{cases} \omega_{re} = \omega_{r\_ref} - \omega_{r\_est} \\ i_{ds\_e} = i_{ds}^* - i_{ds} \\ i_{qs\_e} = i_{qs}^* - i_{qs} \end{cases} \tag{18}$$

The current controller responses of v_{ds}^* and v_{qs}^* are transformed into stationary reference frame voltages ($v_{\alpha s}^*$ and $v_{\beta s}^*$) by using inverse parks transformation as shown in Fig. 1. These reference voltages are fed into the SVPWM technique for the generation of switching pulses.

The FOPI (PI^{λ}) controller is an additional coefficient of the fractional order of integrator (λ). It can make the controller flexible to achieve the desired response. For the approximation of fractional order integration, the well-known Oustaloup approximation method, or CRONE, is deployed [28]. For the appropriate efficacy of IMD, ITSE is taken into consideration as an objective function to assess the optimal coefficients of the controller with minimized $f_o(k)$. It is implemented to obtain the optimal coefficients of the FOPI controller using GOA. The minimized value of the objective function is employed to choose the optimum gain values, which improves drive performance.

$$ITSE = f_o(k) = f_o(k,t) = \int_0^{t_s} e^2(k,t)t\mathrm{d}t \tag{19}$$

where $e(t) = |y(t)_{actual} - y^*(t)_{estimated}|$ represents the error term between the reference and actual, t_s is total simulation time, and r is real positive number.

1) Implementation of FOPI-GOA

The FOPI controllers using GOA are integrated to enhance the dynamic performance of IMD. An optimization process comprises grazing without a predator and running from a spotted predator to heaven. This makes the computational fast with a rapid convergence rate.

The ITSE, k_p, k_i, and λ of speed, and current regulator gain movements in the search space are depicted in Fig. 3(a)–(f) respectively. The convergence curve of optimal tuning of GOA is portrayed in Fig. 3(a), and the optimal best cost function of 0.05632 is accomplished within 24 iterations. The speed, d- and q-axis current controller k_p and k_i gain variations concerning iteration are carried on the same figure with the left and right y-axis as depicted in Fig. 3(b)–(d). The integral coefficient of speed controller (λ_{speed}) variations concerned iterations as depicted in Fig. 3(e). The d- and q-axis current controller λ_{dCC} and λ_{qCC} coefficient variations concerning iteration is carried on a same figure with left and right y-axis as portrayed in Fig. 3(f). It is noticed that the k_p, k_i, and λ gains of speed controller are 27.352, 0.3254 and 0.94134, d-axis current controller is

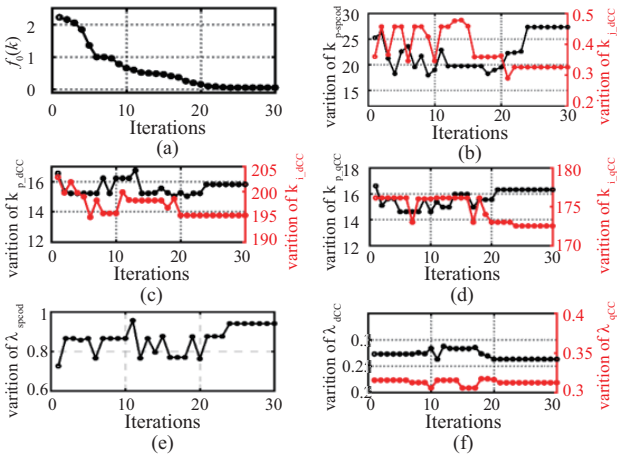

Fig. 3. FOPI gain tuning (a) Convergence curve, variations of k_p, and k_i. (b) Speed controller. (c) d-axis. (d) q-axis current controller, variations of λ. (e) Speed controller. (f) d-axis and q-axis current controller versus iteration.

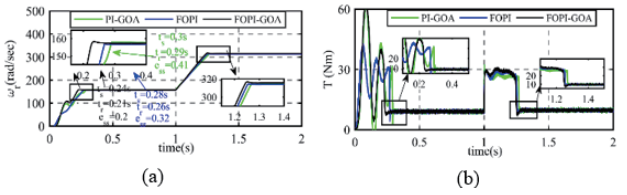

Fig. 4. Performance of (a) speed (ω_r) and (b) electromagnetic torque (T_e) of IMD using PI and FOPI controller.

15.8124, 195.261 and 0.2631, and q-axis current controller is 16.3146, 172.516, and 0.3124.

2) Effectiveness of GOA-Based FOPI Controller in IVC

Optimal values are utilized in the ReTSK-GOA-based PA-IVC strategy of IMD for enhanced drive performance. The dynamic operation characteristics of speed (ω_r) and electromagnetic torque (T_e) are shown in Fig. 4 by utilizing the gain values of PI-GOA, FOPI, and FOPI-GOA. From this, it is observed that the settling time of the FOPI-GOA is 0.24 s only, it is faster as compared to others. Also, very few oscillations with less steady-state error of 0.2 are produced in the system with optimal gains of FOPI. From this, it can be concluded that the optimal values of FOPI controllers produce better dynamic responses as well as faster.

IV. Simulation Results and Discussions

The ReTSK-GOA-based PA-IVC sensorless speed control of the IMD is implemented in MATLAB 2016a for simultaneous parameters and sensorless speed estimation. The designed model is simulated with a sampling time of 20 μs, and the effectiveness of the presented control strategy is validated by considering various dynamic operations of speed and load. A scale-down EVDM is developed in simulation and considered as a load-on induction motor. The parameter specification of this model is implied in the Appendix.

TABLE I
Accuracy Evaluation of Proposed GOA-ReTSK

Parameter	Data	MSE	RMSE	ME	ESD
R_{s_est}	Train	0.016249	0.127471	0.008542	0.12462
	Test	0.018892	0.137448	0.009368	0.13861
R_{r_est}	Train	0.003642	0.0603489	0.002862	0.06184
	Test	0.003009	0.054854	0.001989	0.051932
L_{s_est}	Train	8.5469e-6	0.0029235	8.3249e-5	0.0028591
	Test	8.2613e-6	0.0028742	8.04686e-5	0.0024032
L_{r_est}	Train	7.3146e-6	0.002704	6.9382e-5	0.002138
	Test	6.856e-6	0.002618	5.5321e-5	0.002061
L_{m_est}	Train	0.0001264	0.0112401	1.89062e-5	0.01108
	Test	0.0001153	0.0107368	1.35201e-5	0.010532
ω_{r_est}	Train	1.583e-28	1.2581e-14	2.1362e-16	1.2168e-14
	Test	1.6123e-28	1.2697e-14	2.4703e-16	1.211e-14

A. Performance Assessment Analysis of ReTSK-GOA

The performance behavior and the accurate predictability of the GOA-based ReTSK model are obtained by using various statistical indices such as MSE, RMSE, ME, and standard deviation error (SDE) during training and testing. The predictive system is verified with measured data and statistical solutions; it reveals that the implementation of the GOA-ReTSK approach estimates the accurate parameters. The dataset was randomly divided into data sets of training and testing, to avoid deviance in the learning algorithm. The estimator model performance is also evaluated concerning each target and it confirms the reduced error to achieve the accurate estimation.

The optimization error analysis of the proposed algorithm for training and testing data by considering statistical indices concerning each estimated parameter is obtained and tabulated in Table I, for observation R_s graphs are illustrated in Fig. 5. The best-fitted multi-input multi-output ReTSK-GOA is obtained with the performance indices RMSE for estimation of R_s = 0.127471, R_r = 0.0603489, L_s = 0.00292350, L_r = 0.00270455, L_m = 0.0112401068, and rotor speed is 1.2581e-14 during training; whilst testing R_s = 0.137448, R_r = 0.0548534, L_s = 0.00287424, L_r = 0.00261839, L_m = 0.0107368524, and rotor speed is 1.2697e-14. From Table I, it is observed that the predicted response strongly tracks the test data and training data. It can reveal that the recommended algorithm-based predictive model stipulates the desired response to substantially higher accuracy and lower compilation effort.

B. Performance of ReTSK-GOA-Based IVC-IMD With Dynamic Operation

The performance of the sensorless speed control of the IVC-IMD analysis and the proposed ReTSK-ANF system parameter estimate is described in the section with two portions that have distinct dynamic circumstances, such as variable load and variable speed. For this, the integrated MATLAB system is simulated with 9 s of simulation time. In the first part, the variable speed with constant load operation from 0 to 4.5 s

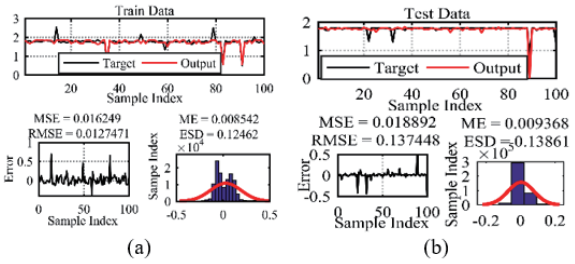

Fig. 5. Optimization error analysis of (a) train and (b) test data of estimated stator resistance.

simulation time and from 4.5 s to 9 s simulation time dynamic load operation with constant speed operation is carried out in the next part simultaneously. Initially, the reference speed ($\omega_{r\text{-}ref}$) is imposed from 0 to 157 rad/s of 50% rated speed at 0.001 s and persistent up to 1.5 s, at time t = 1.5 s of simulation time, the speed is step raised to a rated speed of 314 rad/s, again at t = 3 s of simulation time the reduced to 100 rad/s and maintain same till t = 4.5 s as shown in Fig. 6. But throughout this region, the load T_v on IM is considered as a constant of 12 N·m (by providing the till angle as 40°). At t = 4.5 s, the speed increased to 314 rad/s and maintained constant till t = 9 s of simulation time, but the load on IM is changed for every 1.5 s of time. Initially, at t = 4.5 s it started with no load (approximately 2 N·m, due to inertia), and t = 6 s raised to 50% of the rated load of 10 N·m. Again t = 7.5 s increased to 75% of rated load 15 N·m. Various speeds and loads are randomly considered on IM for analysis of the robustness and performance of IMD with the proposed control strategy. By considering these dynamic operations, the performance validation of adaptive IFOC-IMD using ReTSK-ANF-based parameter estimation is demonstrated in this section.

The performance characteristics of speed ($\omega_{r\text{-}ref}$, $\omega_{r\text{-}act}$, and $\omega_{r\text{-}est}$), estimated electrical parameters of R_s, R_r, L_s, L_r, and L_m, and by adopting the estimated parameters in the IVC strategy for evaluation of drive performance the tuned slip speed (ω_{sl}), actual rotor speed, torque (T_v and T_e) performance waveforms using ReTSK-GOA are illustrated in Fig. 6. The input signals of stationary reference frame stator voltages ($v_{\alpha s}$ and $v_{\beta s}$) and currents ($i_{\alpha s}$ and $i_{\beta s}$), and stator filed orientation (θ_e) are depicted in Fig. 7. The speed characteristics, R_s, R_r, L_s, L_r, L_m, ω_{sl}, ω_e and torque are respectively shown in Fig. 7. It is noticed from Fig. 6 subplot a, the $\omega_{r\text{-}est}$ and by adopting the parameters in IVC the $\omega_{r\text{-}act}$ of IM are strongly tracking the $\omega_{r\text{-}ref}$ during both dynamic speed as well as dynamic load condition. Similarly, from Fig. 6 subplot i the developed T_e of drive follows the T_v. It represents robustness and accuracy of the system. But at the instant of dynamic speed operation, a high amount of transients is developed in T_e. By changing the gradient in EVDM, the dynamic load operation is performed, at instant of dynamic load the smooth operation is carried for development of torque. The torque ripples of the drive using ReTSK-GOA are 2.1 N·m, which means the developed T_e has fewer torque ripples.

The estimated R_s, R_r, L_s, L_r, and L_m parameters using ReTSK-GOA are shown in Fig. 6 subplot b, c, d, e, and f, respectively. For clear observation of transients at the instant of dynamic

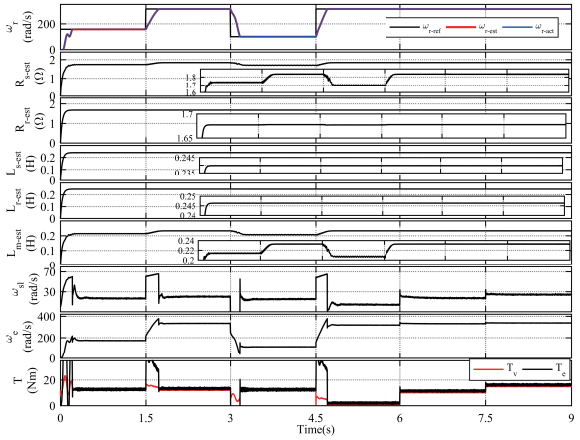

Fig. 6. Performance characteristics of estimated parameters and adaptive IVC-IMD using ReTSK-GOA under dynamic operation.

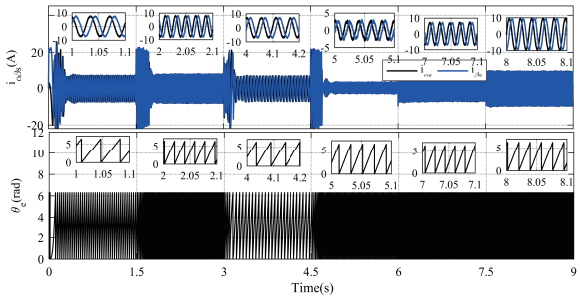

Fig. 7. Performance characteristics of stationary reference frame current and filed orientation of IVC-IMD using ReTSK-GOA under dynamic operation.

operation, the magnified figures are in the same plot. The accurate parameters are estimated with few transients. Since significant transient currents are typically generated at the beginning of IM, the predicted electrical properties are also affected during this period. However, the suggested estimation technique quickly reaches a steady state, indicating the ReTSK-GOA's dependability. Based on mean values, the performance comparison % errors of calculated parameters with real values of IM were assessed. Such as R_s, R_r, L_s, L_r, and L_m are 1.58%, 0.12%, 0.05%, 0.05%, and 1.42%, respectively. From this, it is observed that the estimated values of IM are precise by implementing ReTSK-GOA. The adaptive tuned ω_{sl}, the cumulative slip speed, rotor speed, and the stator filed angular speed ω_e are respectively illustrated in Fig. 6 subplot g and h. Due to the change of load from no load to high load, the slip speed magnitude is increased and the ω_e *is* observed based on the slip speed and rotor speed. By integrating the ω_e, the θ_e is evaluated as shown in Fig. 7 subplot b. The system is working in a closed loop, so the developed θ_e is provided to transform to get the reference stationary reference frame stator voltages. It helps to generate the switching pulses for VSI operation.

The drive performance characteristics of stator currents ($i_{\alpha s}$ and $i_{\beta s}$), and stator filed orientation (θ_e) are respectively depicted in Fig. 7. During dynamic speed operation, the frequency of produced stator currents changes as per $\omega_{r\text{-}ref}$, but the magnitude of currents is constant throughout this operation.

During dynamic load operation, the frequency of produced stator currents is constant, but the magnitude changes linearly with the concerned load. The observation of frequency and magnitude variations in $i_{\alpha\beta s}$ and θ_e the magnified figures are respectively drawn in Fig. 7 subplots a and b. It is observed that for a smaller amount of load lower magnitude of currents was drawn by the IM, and for a higher amount of load the IM drew a higher magnitude of currents. Concerning each dynamic operation region, the field orientation of the drive frequency is also changed and for clear insight, the magnified figures are shown in Fig. 7 subplot b. This leads to the conclusion that the presented estimation-based adaptive control algorithms offer superior dynamic performance for torque and speed across a broad range of variations.

C. Performance of ReTSK-GOA-Based IVC-IMD With Speed Reversal Operation

The step speed reversal operation is performed with 50% of load torque. Initially, +50 rad/s of 10% of rated speed is considered and at t = 1.5 s of simulation time, the speed is changed from +50 to −50 rad/s. The IM's estimated parameters and performance characteristics under speed reversal operation are shown in Fig. 8, including the performance characteristics of speed ($\omega_{r\text{-}ref}$, $\omega_{r\text{-}act}$, and $\omega_{r\text{-}est}$), estimated electrical parameters of R_s, R_r, L_s, L_r, and L_m, tuned slip speed (ω_{sl}), ω_e, torque (T_v and T_e), stator currents ($i_{\alpha s}$ and $i_{\beta s}$), and stator filed orientation (θ_e) performance waveforms using ReTSK-GOA. It was noticed from Fig. 8 subplot a, the $\omega_{r\text{-}est}$ and by adopting the parameters in IRFOC the $\omega_{r\text{-}act}$ of IM are strongly tracking the $\omega_{r\text{-}ref}$ during speed reversal condition. Similarly, from Fig. 8 subplot i, the developed T_e of drive follows the T_v. It represents robustness and accuracy of the system. But at the instant of dynamic operation, a high amount of transient's is developed in torque. The estimated parameters of R_s, R_r, L_s, L_r, and L_m are respectively portrayed in Fig. 8 subplot b, c, d, e, and f. The parameters are estimated with few transients and high in R_s and L_m due to low-speed operation.

For clear observation, the zoomed figures are plotted in the same. An adaptive ω_{sl} and ω_e are shown in Fig. 8 subplot g and h respectively. During speed reversal the frequency of generated stator currents is changes as per $\omega_{r\text{-}ref}$, but the magnitude of currents is constant throughout this operation because the load on the IM is considered as constant. The frequency variations in $i_{\alpha\beta s}$ and θ_e can be noticed in Fig. 8 subplot j and k.

From the above dynamic speed, dynamic load, and speed reversal scenarios, the ReTSK-GOA-based parameter adaptive IVC strategy using a fractional PI controller of IMD has achieved excellent dynamic performance with smooth speed control. It is observed that for a wide-range speed operation, the presented control strategy is suitable. Additionally, the proposed control strategy revealed lower overshoot and minimized estimated electrical parameters and speed error.

V. Experimental Results and Discussions

An experimental platform using a dSPACE Micro Lab Box processor has been developed to validate the proposed ReTSK-GOA-based Parameter Adaptive IVC strategy. The setup includes an induction motor with a brake load mechanism, a voltage source inverter with a diode bridge rectifier, the Micro Lab Box processor, voltage and current sensors, a three-phase variac, a DC power supply, and a host system. The system parameters are listed in the Appendix. Stator voltage and current are sensed via LV25-P and LA55-P sensors and fed to the processor through ADCs. Switching pulses are sent to the VSI through an opto-coupler. Test results from various dynamic operations are recorded using a four-channel DSO and presented in the subsequent sections.

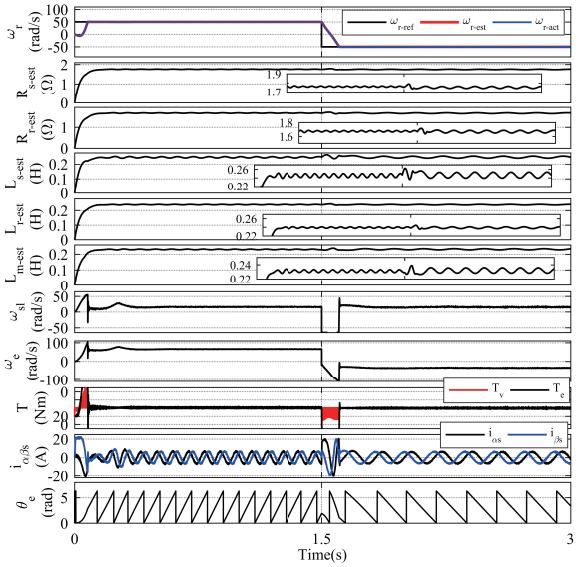

Fig. 8. Performance characteristics estimated parameters and adaptive IVC-IMD using ReTSK-GOA under speed reversal operation.

A. Dynamic Speed Performance of PA-IVC-IMDs

For the dynamic speed operation, the step changes are made in reference speed (ω_{r_ref}) of the drive to analyze the robustness of the control algorithm. The induction motor's sensorless speed control and parameter estimation are performed by the ReTSK-ANF model, which has been trained on GOA. The estimated waveforms and performance analysis during these speed variations are demonstrated in this section. Initially, the ω_{r_ref} of the drive is set as 157 rad/s persistent up too few cycles, then increased to a rated speed of 314 rad/s, then reduced to 100 rad/s. During this operation, the load on the motor is kept constant as 50% of the full load.

The speed and torque performance characteristics of ω_{r_ref}, ω_{r_act}, ω_{r_est}, and T_e IMD during dynamic speed operation is illustrated in Fig. 9. It was noticed that the ω_{r_est}, and ω_{r_act} is closely following the reference during various speed operations. It is observed through the recorded DSO waveform. The approximate value of T_e is equal to 12 N·m. At the instant of dynamics, only the transients are generated due to sudden speed changes. The estimated parameters of IMD are portrayed in Fig. 10, including ω_{r_est}, R_{s_est}, R_{r_est}, L_{m_est}, ω_{r_est}, L_{s_est}, L_{r_est},

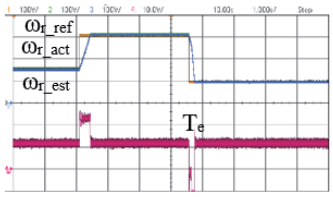

In *x*-axis: 1s/div; In *y*-axis: Ch_1, Ch_2, Ch_3-100V/div, Ch_4-10V/div.

Fig. 9. IMD performance characteristics of ω_{r_ref}, ω_{r_act}, ω_{r_est}, and T_e during dynamic speed operation.

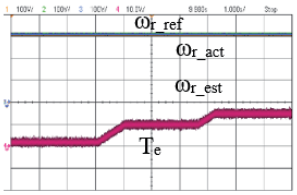

In *x*-axis: 1s/div; In *y*-axis: Ch_1, Ch_2, Ch_3-100V/div, Ch_4-10V/div.

Fig. 12. Performance (ω_{r_ref}, ω_{r_act}, ω_{r_est}, and T_e) of IMD during dynamic load operation.

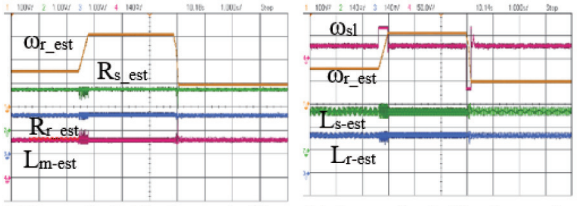

(a) In *x*-axis: 1s/div; In *y*-axis: Ch_1-100V/div, Ch_2, Ch_3-1V/div, Ch_4-140mV/div. (b) In *x*-axis: 1s/div; In *y*-axis: Ch_1-100V/div, Ch_2, Ch_3-140mV/div, Ch_4-50V/div.

Fig. 10. Estimated parameters of IMD during dynamic speed operation (a) ω_{r_est}, R_{s_est}, R_{r_est}, L_{m_est}, and (b) ω_{r_est}, L_{s_est}, L_{r_est}, ω_{sl}.

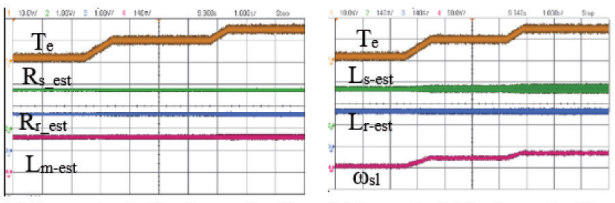

(a) In *x*-axis: 1s/div; In *y*-axis: Ch_1-10V/div, Ch_2, Ch_3-1V/div, Ch_4-140mV/div. (b) In *x*-axis: 1s/div; In *y*-axis: Ch_1-10V/div, Ch_2, Ch_3-140mV/div, Ch_4-50V/div.

Fig. 13. performance of (a) T_e, R_{s_est}, R_{r_est}, L_{m_est} and (b) T_e, L_{s_est}, L_{r_est}, ω_{sl} IMD during dynamic load operation.

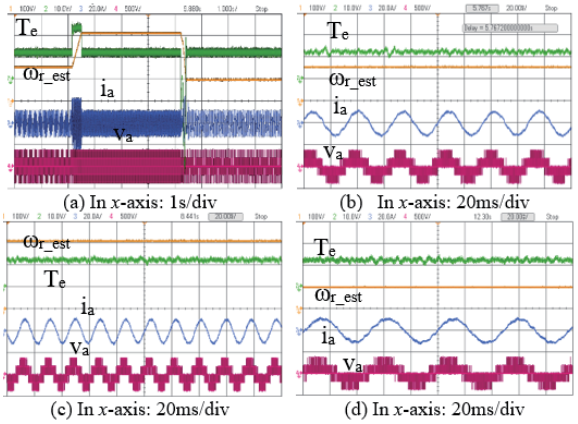

(a) In *x*-axis: 1s/div (b) In *x*-axis: 20ms/div (c) In *x*-axis: 20ms/div (d) In *x*-axis: 20ms/div

Fig. 11. Performance characteristics (ω_{r_est}, T_e, i_a and v_a) of IMD during dynamic speed operation (In *y*-axis: Ch_1-100 V/div, Ch_2-10 V/div, Ch_3-20 A/div, Ch_4-500 V/div).

and ω_{sl}. Due to change of speed, the frequency developed in stator current changes, then the L_{m_est} is value varied. During the rated speed of operation, the L_{m_est} is measured as near to the actual, but other than the rated speed it's estimated as lower due to change of frequency. Insignificant transients are generated during the time of dynamics operation in estimated parameters, but it reaches the steady-state quickly. The ω_{sl} is evaluated mathematically and fetched into stator field orientation by adopting these estimated parameters in the IVC strategy. Due to few ripples in the estimated parameters, the slip speed also consists few negligible ripples.

The characteristics of ω_{r_est}, T_e, stator current of phase a (i_a), and stator voltage of phase a (v_a) of IM is depicted in Fig. 11(a). For clear observation the performance characteristics of ω_{r_est}, T_e, i_a and v_a of IMD zoomed figures for ω_{r_ref} of 157, 314, and 100 rads/s respectively imposed in the Fig. 11(b)–(d) with 20 ms/div scale. This indicates that the VSI-generated stator current, has a frequency of 50 Hz across the rated speed range and varies based on operating speed. During this operation, the stator current of the IM is constant because the load on the IM is constant.

B. Dynamic Load Performance of PA-IVC-IMD

The dynamic load operation is carried out in this subsection to analyze the robustness of a GOA-integrated ReTSK-ANF model. For the dynamic load operation, various loads are applied such as no-load (0%), 50%, and 75% of rated load by using brake load mechanism. The ω_{r_ref} is considered as constant throughout this operation as 314 rad/s.

The speed and torque performance characteristics of ω_{r_ref}, ω_{r_act}, ω_{r_est}, and T_e IMD during dynamic speed operation is illustrated in Fig. 12. From this figure it was noticed that the ω_{r_est}, and ω_{r_act} is closely following the reference during various speed operations. It is measured in DSO approximately equal to 2, 10, and 15 N·m respectively. The estimated parameters of IMD are illustrated in Fig. 13, including T_e, R_{s_est}, R_{r_est}, L_{s_est}, and T_e, L_{r_est}, L_{m_est}, ω_{sl}. Due to change of load, the ripples in estimated parameters is increases due to temperature effect and magnetization. By adopting the estimated parameters in the IVC, the ω_{sl} of is evaluated mathematically and fetched into stator field orientation. It can be utilized for Clarks and Park's transformation in IVC.

The performance characteristics of ω_{r_est}, T_e, stator current of phase a (i_a), and stator voltage of phase a (v_a) of IM are depicted in Fig. 14(a). For clear observation the performance characteristics of ω_{r_est}, T_e, i_a and v_a of IMD zoomed figures for each load respectively imposed in Fig. 14(b)–(d) with 20 ms/div scale. It

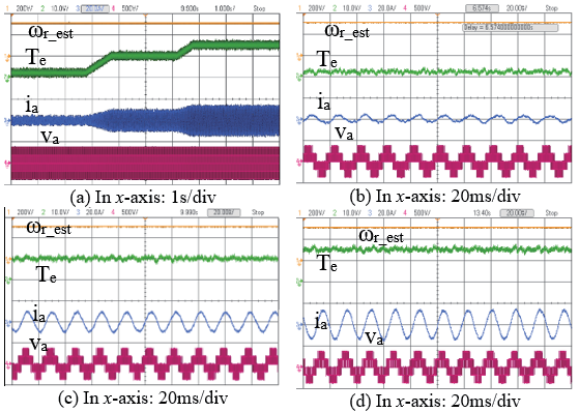

Fig. 14. Performance characteristics of ω_{r_est}, T_e, i_a and v_a of IMD during dynamic load operation (In y-axis: Ch_1-200 V/div, Ch_2-10 V/div, Ch_3-20 A/div, Ch_4-500 V/div).

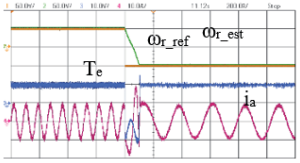

Fig. 15. Performance of ω_{r_ref}, ω_{r_est}, T_e, and i_a of IMD response during speed reversal operation. In the x-axis: 200 ms/div; In y-axis: Ch_1, Ch_2-50 V/div, Ch_3-10 V/div, Ch_4-10 A/div.

observed from this, the generated supply current from VSI has approximately 50 Hz of frequency throughout this operation as per ω_{r_ref}, but the magnitude of current is changed proportionally as load.

C. Performance of PA-IVC-IMD During Speed Reversal

Further, the GOA-based ReTSK-ANF model is employed for the estimation of parameters and sensorless speed of IM, and the estimated waveforms and performance analysis during dynamic speed reversal are demonstrated. The speed reversal operation is performed with speeds of ±50 rad/s by considering the half of the load on the motor. An IMD performance characteristics of ω_{r_ref}, ω_{r_est}, T_e, and i_a are portrayed in Fig. 15. During speed reversal operation, the ω_{r_est} strongly tracks the ω_{r_ref}. The estimated parameters ω_{r_est}, R_{s_est}, R_{r_est}, L_{m_est}, and ω_{r_est}, L_{s_est}, L_{r_est}, ω_{sl} are shown in Fig.16.

From the above various operating analysis, the ReTSK-GOA-based parameter adaptive IVC strategy of IMD has achieved excellent dynamic performance with smooth speed control. Additionally, the proposed control strategy revealed lower overshoot and minimized estimated electrical parameters and speed error.

VI. Conclusion

Parameter adaptive sensorless speed IVC of IMD along with accurate parameter estimation using ReTSK-GOA is proposed

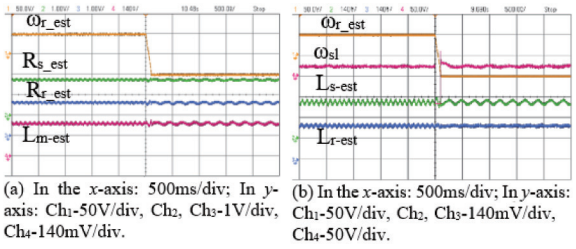

Fig. 16. Estimated parameters of IMD during speed reversal operation (a) ω_{r_est}, R_{s_est}, R_{r_est}, L_{m_est}, and (b) ω_{r_est}, L_{s_est}, L_{r_est}, ω_{sl}.

in this work. The metaheuristic GOA is adopted for constructing the predictive model of ReTSK-ANF and for obtaining the optimal gains of the fractional order PI controller. The ReTSK-GOA optimizes the fuzzy rules and membership functions for accurate estimation and performance enhancement of the drive. The statistical indices of MSE, RMSE, EM, and ESD, during the training stage, were 3.33e-3, 3.41e-2, 1.92e-3, 3.37e-2 and during the testing stage 3.67e-3, 3.47e-2, 1.91e-3, 3.42e-2 are reported. This confirms that the ReTSK-ANF estimator significantly improves parameter estimation, ensuring that the estimated motor speed closely matches the actual speed and aligns with the reference. It is tested under a wide range of dynamic variations. Owing to efficient smooth control over the variable speed and load as well as at a very low speed, it must be suitable for EV applications. The GOA achieved stable FOPI gains with the best cost function of 0.05632. The recorded response signifies the GOA-based approach offers enhanced transient response with a fast-settling time. The proposed estimation-based adaptive control strategy is validated using MATLAB/Simulation and the developed hardware prototype ensures satisfactory robustness with accurate estimation and stable operation of the system under dynamic operating conditions with lesser transients and settling time.

Appendix

Specification of parameters: Rated voltage = 415 V, supply frequency F = 50 Hz, rated power = 5 hp, inertia constant J = 0.011 kg/m^2, No. of poles = 4, switching frequency F_s = 4.8 kHz, stator resistance R_s = 1.78 Ω, rotor resistances R_r = 1.68 Ω, mutual inductance L_m = 0.009 H, stator leakage inductance L_{ls} = 0.2363 H, rotor leakage inductance L_{lr} = 0.2363 H.

References

[1] Y. Beddiaf, F. Zidani, and S. Drid, "Modified speed sensorless indirect field-oriented control of induction motor drive," in *International Journal of Modelling, Identification*, vol. 25, no.4, pp. 273–286, 2016.

[2] R. De Doncker, D. W. J. Pulle, and A. Veltman, *Advanced Electrical Drives: Analysis, Modeling, Control*, 2nd edition, Springer, Berlin, Germany, 2020, pp. 285–337.

[3] S. A. Davari, D. A. Khaburi, and R. Kennel, "An improved FCS-MPC algorithm for an induction motor with an imposed optimized weighting factor," in *IEEE Transactions on Power Electronics,* vol. 27, no. 3, pp. 1540–1551, Mar. 2012.

[4] Y. Mei and G. Yi, "Advanced model predictive current control for induction motor drive system fed by indirect matrix converter," in *Journal of Power*

Electronics, vol. 20, pp. 466–478, 2020.
[5] A. Kacenka, P. Makys, and L. Struhamansky, "Impact of parameter variation on sensorless indirect field oriented control of induction machine," in *Lecture Notes in Electrical Engineering*, pp. 799–809, Jan. 2020.
[6] M. S. Sepeeh, S. A. Zulkifli, S. Y. Sim, H. J. Chiu, and M. Z. C. Wanik, "Speed tracking for IFOC induction motor speed control using hybrid sensorless speed estimator based on flux error for electric vehicles application," in *Journal of Machines*, vol. 10, no. 11, pp. 1089, Nov. 2022.
[7] P. Cao, X. Zhang, and S. Yang, "A unified-model-based analysis of MRAS for online rotor time constant estimation in an induction motor drive," in *Transactions on Industrial Electronics*, vol. 64, no. 6, pp. 4361–4371, Jun. 2017.
[8] D. Dong, W. Xu, X. Xiao, Y. Tang, and K. Yang, "Online identification strategy of secondary time constant and magnetizing inductance for linear induction Motors," in *IEEE Transactions on Power Electronics*, vol. 37, no. 10, pp. 12450–12462, Oct. 2022.
[9] S. H. Lee, A. Yoo, H. J. Lee, Y. D. Yoon, and B. M. Han, "Identification of induction motor parameters at standstill based on integral calculation," in *IEEE Transactions on Industry Applications,* vol. 53, no. 3, pp. 2130–2139, May 2017.
[10] F. Baneira, L. Asiminoaei, H. A. M. Delpino, and J. Godbersen, "Estimation method of stator winding resistance for induction motor drives based on DC-signal injection suitable for low inertia," in *IEEE Transactions on Power Electronics,* vol. 34, no. 6, pp. 5646–5654, Jun. 2019.
[11] E. Armando, A. Boglietti, and S. Rubino, "Flux-decay test: A viable solution to evaluate the induction motor rotor time-constant," in *IEEE Transactions on Industry Applications,* vol. 57, no. 4, pp. 3619–3631, Jul. 2021.
[12] A. Dineva, A. Mosavi, S. F. Ardabili, and K.W. Chau, "Review of soft computing models in design and control of rotating electrical machines," in *Journal of Energies,* vol. 12, no. 6, pp. 1049, 2019.
[13] M. M. Hasan, "Artificial neural network based speed estimator for sensorless field-oriented control of three phase induction motor," in *Proceedings of 3rd International Conference on Electrical, Computer & Telecommunication Engineering (ICECTE),* Bangladesh, pp. 57–60, 2019.
[14] O. Cetin, A. Dalcali, and F. Temurtas, "A comparative study on parameters estimation of squirrel cage induction motors using neural networks with unmemorized training," in *International Journal of Engineering Science and Technology,* vol. 23, no. 5, pp. 1126–1133, 2020.
[15] T. Banerjee and J. N. Bera, "An improved torque ripple reduction controller for smooth operation of induction motor drive," in *Journal of Control, Automation and Electrical Systems,* vol. 34, pp. 247–264, Sept. 2022.
[16] F. Zidani and M. E. H. Benbouzid, "A fuzzy method for rotor time constant estimation for high-performance induction motor vector control," in *Journal of Electric Power Components and Systems,* vol. 31, no. 10, pp. 1007–1019, 2003.
[17] D. Karaboga and E. Kaya, "Adaptive network-based fuzzy inference system training approaches a comprehensive survey," in *Journal of Artificial Intelligence Revolution,* vol. 52, pp. 2263–2293, 2019.
[18] E. K. P. Chong and S. H. Zak, *An Introduction to Optimization: With Applications to Machine Learning*, 5th Edition, Wiley, Sept. 2023, pp. 517–623.
[19] M. R. Mosavi, A. Ayatollahi, and S. Afrakhte, "An efficient method for classifying motor imagery using CPSO-trained ANFIS prediction," in *Journal of Evolving Systems,* vol. 12, pp. 319–336, 2021.
[20] K. Premkumar and B. V. Manikandan, "GA-PSO optimized online ANFIS-based speed controller for BLDC motor," in *Journal of Intelligent and Fuzzy Systems,* vol. 28, no. 6, pp. 2839–2850, Feb. 2015.
[21] S. Gu, Y. Chou, J. Zhou, Z. Jiang and M. Lu, "Takagi–Sugeno–Kang fuzzy clustering by direct fuzzy inference on fuzzy rules," in *IEEE Transactions on Emerging Topics in Computational Intelligence*, vol. 8, no. 2, pp. 1264–1279, Apr. 2024.
[22] A. Abdollahpour, A. Rouhi, and E. Pira, "An improved gazelle optimization algorithm using dynamic opposition-based learning and chaotic mapping combination for solving optimization problems," in *Journal of Supercomputing*, vol. 80, pp. 12813–12843, Feb. 2024.
[23] S. B. Joseph, E. G. Dada, A. Abidemi, and B. M. Khammas, "Metaheuristic algorithms for PID controller parameters tuning: Review, approaches, and open problems," in *Journal of Heliyon* vol. 8, no.5, May 2022.
[24] S. Singh, V. K. Tayal, H. P. Singh, and V. K. Yadav, "Design of PSO-tuned FOPI & Smith predictor controller for nonlinear polymer electrolyte membrane fuel cell," in *Journal of Energy Sources, Part A: Recovery, Utilization, and Environmental Effects*, pp. 1–22, 2022.
[25] S. Ekinci, B. Hekimoglu, A. Demiroren, and S. Kaya, "Harris Hawks optimization approach for tuning of FOPID controller in DC-DC buck converter," in *Proceedings of 2019 International Artificial Intelligence and Data Processing Symposium (IDAP)*, Malatya, Turkey, pp. 1–9. 2019.
[26] M. K. Kar, S. Kumar, A. K. Singh, and M. Cherukuri, "Design and analysis of FOPID-based damping controllers using a modified grey wolf optimization algorithm," in *International Transactions on Electrical Energy Systems,* vol. 2022, pp. 1–31, Oct. 2022.
[27] J.O. Agushaka, A.E. Ezugwu, and L. Abualigah, "Gazelle optimization algorithm: A novel nature-inspired metaheuristic optimizer," in *Journal of Neural Computing and Applications,* vol. 35, pp. 4099–4131, 2023.
[28] W. Zheng, Y. Chen, X. Wang, and J. Guo "Robust fractional order PID controller synthesis for the first order plus integral system," in *Journal of Measurement and Control,* vol. 56, no. 2, pp. 202–214, 2023.

Pudari Mahesh received the B.T. in degree electrical and electronics engineering from JNTU, Hyderabad, India, in 2014 and M.Tech. degree in electrical engineering with specialization of power electronics from Kakatiya University, India, in 2016. In January 2016, he joined as an Assistant Professor in Electrical and Electronics Engineering Department, KITSW College, Warangal, India. Since August 2020, he is pursuing Ph.D. degree in electrical engineering from Sardar Vallabhbai National Institute of Technology, Surat, India. His research area includes power electronics, parameter estimation and sensorless speed control of electric drives.

Sabha Raj Arya received B.E. degree in electrical engineering from Government Engineering College Jabalpur, in 2002, Master of technology in power electronics from Motilal National Institute of Technology, Allahabad, in 2004 and Ph.D. degree in electrical engineering from Indian Institute of Technology (I.I.T) Delhi, New Delhi, India, in 2014. He joined the Department of Electrical Engineering, Sardar Vallabhbhai National Institute of Technology, Surat, as Assistant Professor and became Associate Professor, Professor in 2019, 2023 respectively in same institute. His areas of interest include power quality, power electronics, power filter design, design of dc/dc converters and distributed power generation. He is a recipient of Two National Awards, namely the INAE Young Engineer Award from the Indian National Academy of Engineering and the POSOCO Power System Award from the Power Grid Corporation of India in 2014 for his research work. He also received the Amit Garg Memorial Research Award-2014 from I.I.T Delhi for high-impact publication in a quality journal during the session 2013–2014. In the year 2023, he has received Tata Rao Price from Institution of Engineer (IE), India for his research paper. He has published more than one hundred fifty research paper in journals and conferences in the field of electrical power quality and power electronics. He also serves as an Associate Editor for the *IET (U.K.) Renewable Power Generation*.